ACS OMEGA

http://pubs.acs.org/journal/acsodf

Article

Perfect Spherical Tetrahedral Metallo-Borospherene Ta_4B_{18} as a Superatom Following the 18-Electron Rule

Yu Zhang, Xiao-Qin Lu, Miao Yan, and Si-Dian Li*

Cite This: https://doi.org/10.1021/acsomega.1c00828

Read Online

ABSTRACT: Cage-like metallo-borospherenes exhibit unique structures and bonding. Inspired by the newly reported smallest spherical trihedral metallo-borospherene D_{3h} $Ta_3B_{12}^-$ (**1**), which contains two equivalent B_3 triangles interconnected by three B_2 units on the cage surface, we present herein a first-principles theory prediction of the perfect spherical tetrahedral metallo-borospherene T_d Ta_4B_{18} (**2**), which possesses four equivalent B_3 triangles interconnected by six B atoms, with four equivalent nonacoordinate Ta centers in four η^9-B_9 rings as integrated parts of the cage surface. As the well-defined global minimum of the neutral, Ta_4B_{18} (**2**) possesses four 10c-2e $B_9(\pi)$−$Ta(d_\sigma)$ and eight 10c-2e $B_9(\pi)$−$Ta(d_\delta)$ coordination bonds evenly distributed over four Ta-centered $Ta@B_9$ nonagons, with the remaining 18 valence electrons in nine 22c-2e totally delocalized bonds following the 18-electron principle ($1S^21P^61D^{10}$) of a superatom. Such a bonding pattern renders spherical aromaticity to the tetrahedral complex, which can be used as building blocks to form the face-centered cubic crystal Ta_4B_{15} (**3**). The IR, Raman, and UV−vis spectra of Ta_4B_{18} (**2**) are theoretically simulated to facilitate its future experimental characterizations.

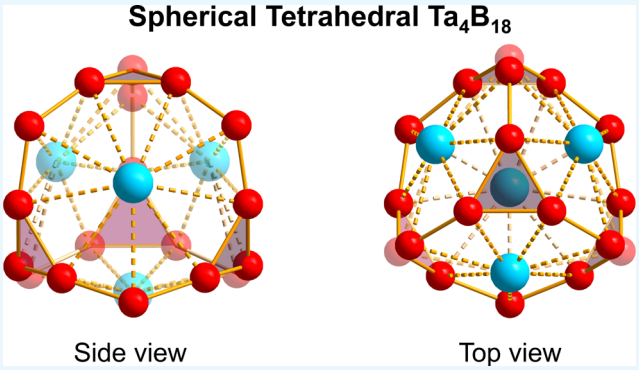

INTRODUCTION

Boron as a prototypical electron-deficient element exhibits unique structures and bonding in bulk allotropes, polyhedral molecules, and gas-phase clusters.[1−3] Combined photoelectron spectroscopy (PES) and first-principles theory investigations in the past two decades have unveiled a rich landscape for size-selected boron clusters ($B_n^{-/0}$) from planar or quasi-planar species (n = 3−38, 41, and 42) to cage-like borospherenes (C_3/C_2 B_{39}^- and D_{2d} $B_{40}^{-/0}$) featuring delocalized multicenter two-electron (mc-2e) σ and π bonds, with B_{39}^- being the only boron cluster monoanion possessing a cage-like global minimum (GM).[2−9] Seashell-like C_2 $B_{28}^{-/0}$ and C_s B_{29}^- were later observed in PES measurements as minor isomers coexisting with their quasi-planar GM counterparts.[7,8] Endohedral $M@B_{40}$ (Ca, Sr, Sc, Y, and La) and exohedral $M\&B_{40}$ (M = Be and Mg) metallo-borospherenes were proposed in theory shortly after the discovery of D_{2d} $B_{40}^{-/0}$.[10,11] Endohedral D_2 $Ta@B_{22}^-$ and D_{2d} $U@B_{40}$ were predicted to be superatoms following the 18-electron rule and 32-electron principle, respectively.[12,13] Other cage-like B_n clusters (n = 20, 30, 38, 40, 50, and 60) and related Ti-doped species have also been predicted in theory.[14,15] Joint ion-mobility measurements and density functional theory (DFT) investigations indicated that B_n^+ boron cluster monocations possess double-ring tubular structures in the size range between n = 16 and 25.[16] Extensive GM searches and DFT calculations showed that B_{46} is the smallest core−shell boron cluster with a B_4 core at the center ($B_4@B_{42}$), while B_{48}, B_{54}, B_{60}, and B_{62} are the first bilayer boron clusters predicted to date.[17,18] Encouragingly, bilayer $B_{48}^{-/0}$ has been very recently confirmed in gas-phase PES measurements, revealing a new structural domain in boron nanoclusters and nanomaterials.[19]

Transition metal-doping generates interesting structures and bonding in boron clusters. Typical examples include the experimentally confirmed monometal-centered boron wheels $M@B_n$ ($Co@B_8^-$, $Ru@B_9^-$, and $Ta@B_{10}^-$), double-ring tubular boron drums $M@B_n^-$ ($Mn@B_{16}^-$, $Co@B_{16}^-$, $Rh@B_{18}^-$, and $Ta@B_{20}^-$), and di-metal-doped inverse-sandwich D_{6h} $Ta_2\&B_6^{-/0}$.[20−26] Di-La-doped inverse-sandwich-type mono-decker $La_2B_n^-$ (n = 7−9)[27,28] and tri-La-doped inverse triple-decker $La_3B_{14}^-$ were also observed in PES experiments.[29] Double-ring tubular C_{2h} La_2B_{20} ($La_2[B_2@B_{18}$) was predicted to be a molecular rotor with fluxional bonds at room temperature.[30] The first tri-La-doped spherical trihedral metallo-borospherene D_{3h} $La_3B_{18}^-$ with three decacoordinate La centers as integral parts of the cage surface has been discovered recently in a combined experimental and theoretical investigation.[31] The

Received: February 15, 2021
Accepted: April 2, 2021

first core–shell spherical trihedral metallo-borospherene D_{3h} $La_3B_{20}^-$ ($La_3[B_2@B_{18}]^-$) with a B_2 core was predicted shortly after.[32] The smallest tri-Ta-doped spherical trihedral metallo-borospherene D_{3h} $Ta_3B_{12}^-$ (**1**) has been very recently predicted by our group, which consists of two eclipsed B_3 triangles on the top and bottom interconnected by three B_2 units on the waist.[33] However, there have been no experimental or theoretical evidence reported on tetra-Ta-doped boron clusters to date. Tetra-metal-doped endohedral metallo-silicon fullerenes T_d M_4Si_{28} (M = Al and Ga) have been theoretically proposed to possess the same tetrahedral symmetry as their fullerene counterpart T_d C_{28}.[34,35] It is natural to ask at the current stage what GM structures the smallest tetra-Ta-doped boron fullerenes may have and if perfect spherical tetrahedral metallo-borospherenes are favored in thermodynamics over their alternative counterparts.

Based on extensive GM searches and first-principles theory calculations, we predict herein the perfect spherical tetrahedral metallo-borospherene T_d Ta_4B_{18} (**2**), which possesses four equivalent B_3 triangles at four corners interconnected by six B atoms on the edges, with four equivalent nonacoordinate Ta centers in four η^9-B_9 rings as integral parts of the cage surface, in the same tetrahedral symmetry as its fullerene counterpart T_d C_{28}.[35] The spherically aromatic Ta_4B_{18} (**2**) possesses one 10c-2e $B_9(\pi)$–$Ta(d_\sigma)$ bond and two 10c-2e $B_9(\pi)$–$Ta(d_\delta)$ coordination bonds over each $Ta@B_9$ nonagon, with the remaining 18 valence electrons in nine 22c-2e bonds following the 18-electron rule ($1S^21P^61D^{10}$). Ta_4B_{18} (**2**) can be used as building blocks to form the face-centered three-dimensional (3D) Ta_4B_{15} (**3**), which is metallic in nature.

RESULTS AND DISCUSSION

Structures and Stabilities. Inspired by the newly reported smallest tri-metal-doped spherical trihedral metallo-borospherene D_{3h} $Ta_3B_{12}^-$ (**1**),[33] which contains two equivalent B_3 triangles interconnected by three B_2 units on the waist, with three octacoordinate Ta centers as integral parts of the cage surface, we manually designed the tetra-metal-doped perfect spherical tetrahedral metallo-borospherene T_d Ta_4B_{18} (**2**) ($^1A_1$), which possesses four equivalent B_3 triangles interconnected by six B atoms on the edges, with four nonacoordinate Ta centers in four η^9-B_9 rings as integrating parts of the cage surface (Figure 1). Interestingly and encouragingly, extensive TGMin GM searches[36,37] show that Ta_4B_{18} (**2**) is the well-defined GM of the neutral complex lying 1.04 eV lower than the second lowest-lying isomer C_s Ta_4B_{18} ($^1A'$) at the CCSD(T)[38−40] level. All the other low-lying cage-like isomers appear to be at least 1.07 eV less stable than the GM in thermodynamics (Figure S1). The first slightly distorted triplet D_2 Ta_4B_{18} ($^3B_2$) is found to lie 1.08 eV higher than the T_d GM at CCSD(T). A similar situation exists in Nb_4B_{18} for which the perfect tetrahedral T_d Nb_4B_{18} also appears to be the well-defined GM of the neutral (Figure 2 and Figure S2). Ta_4B_{18} (**2**) possesses the optimized B–B bond lengths of r_{B-B} = 1.56 between the B_3 triangles at the corners and bridging B atoms on the edges, r'_{B-B} = 1.69 Å within the B_3 triangles, and an average Ta–B coordination bond length of r_{Ta-B} = 2.35 Å between Ta atoms and their η^9-B_9 ligands. The large energy gaps between the highest occupied molecular orbitals (HOMOs) and lowest unoccupied molecular orbitals (LUMOs) of ΔE_{gap} = 2.63 and 2.60 eV calculated for T_d Ta_4B_{18} and T_d Nb_4B_{18}, respectively, well support their high chemical stabilities, similar to the situations observed in cage-like D_{2d} B_{40} and C_3/C_2 B_{39}^-.[4,5]

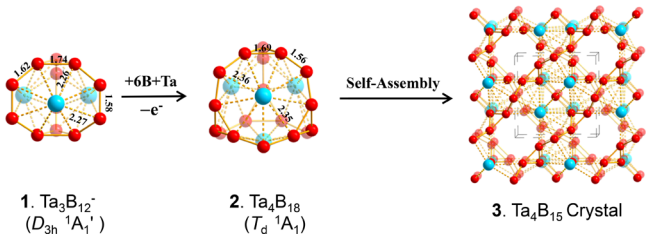

Figure 1. Optimized structures of $Ta_3B_{12}^-$ (**1**), Ta_4B_{18} (**2**), and 3D Ta_4B_{15} crystal (**3**), with bond lengths indicated in Å in **1** and **2** at the PBE0 level.

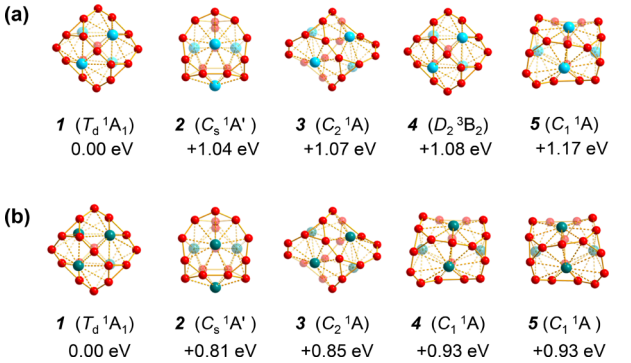

Figure 2. Five lowest-lying isomers of (a) Ta_4B_{18} and (b) Nb_4B_{18} with the relative energies indicated in eV at the CCSD(T) level.

Extensive molecular dynamics (MD) simulations indicate that Ta_4B_{18} (**2**) is also highly dynamically stable, as evidenced by its small calculated average root-mean-square-deviation of RMSD = 0.12 Å and a maximum bond length deviation of MAXD = 0.41 Å at 1500 K (Figure S3a). Similarly, T_d Nb_4B_{18} possesses a small calculated average root-mean-square-deviation of RMSD = 0.12 Å and a maximum bond length deviation of MAXD = 0.36 Å at 1200 K (Figure S3b). These highly stable tetra-Ta-doped spherical tetrahedral metallo-borospherenes possess the same tetrahedral symmetry as their carbon fullerene counterpart T_d C_{28}.[35] T_d Ta_4B_{18} (**2**) can be further self-assembled into the face-centered crystal Ta_4B_{15} (**3**) (P-43m) in which each face-centering B atom is shared by two neighboring cubic unit cells, as shown in Figure 1. Ta_4B_{15} (**3**) possesses the optimized lattice parameters of $a = b = c$ = 5.77 Å at the PBE level,[42] with both the B–B and B–Ta distances remaining basically unchanged compared to the corresponding bond length values in T_d Ta_4B_{18} (**2**). The face-centering B atoms in Ta_4B_{15} (**3**) are tetrahedrally coordinated, forming tetrahedral $B(B)_4$ local structures with a B–B bond length of 1.57 Å. The calculated band structures of Ta_4B_{15} (**3**) indicate that the face-centered 3D crystal is metallic in nature (Figure S4). Its projected density of states (PDOS) shows that both the B-2p orbitals and the Ta-5d orbitals contribute to the calculated PDOS near the Fermi level, with the former making major contributions to the PDOS above the Fermi level while the latter dominating the PDOS below the Fermi level.

Natural Bonding Orbital and Bonding Pattern Analyses. The high stability of T_d Ta_4B_{18} (**2**) originates from its unique structural and bonding patterns. Detailed natural bonding orbital (NBO) analyses show that the four equivalent nonacoordinate Ta atoms in Ta_4B_{18} (**2**) possess the natural

https://doi.org/10.1021/acsomega.1c00828
ACS Omega XXXX, XXX, XXX−XXX

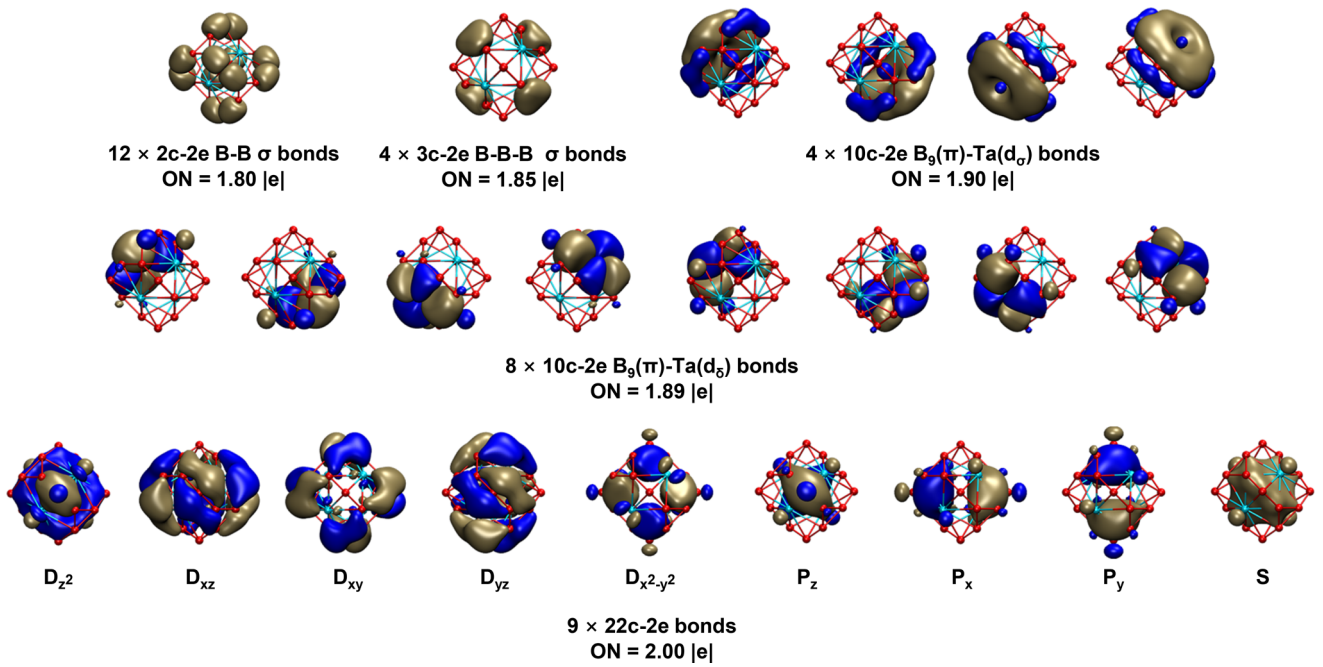

Figure 3. AdNDP bonding patterns of T_d Ta_4B_{18} (**2**), with the occupation numbers (ONs) indicated.

atomic charges of q_{Ta} = +0.94 |e|, electronic configurations of Ta[Xe]$6s^{0.23}5d^{3.74}$, total Wiberg bond indexes of WBI_{Ta} = 5.22, and Ta−B coordination bond orders of WBI_{Ta-B} = 0.41−0.45 (Ta−B interactions within the quasi-planar Ta@B_9), indicating that each Ta atom donates its $6s^2$ electrons almost completely to the η^9-B_9 ligands while in return accepts roughly one electron (≈0.74 |e|) in its partially filled 5d orbitals from the surrounding B_9 ligand via effective B(2p) → Ta(5d) backdonations. Such Ta−B coordination interactions appear to be comparable with those in the previously reported D_{3h} $Ta_3B_{12}^-$, which has the Ta−B coordination bond order of WBI_{Ta-B} = 0.50−0.53 (Ta−B interactions within the Ta@B_8 octagonal pyramids).[33]

Detailed adaptive natural density partitioning (AdNDP)[43,44] bonding analyses shown in Figure 3 unveil both the localized and delocalized bonds of the system. T_d Ta_4B_{18} (**2**) possesses 12 equivalent 2c-2e B−B σ bonds between four B_3 triangles at the corners and six bridging B atoms on the edges and four equivalent 3c-2e σ bonds on four B_3 triangles in the first row and 12 10c-2e B_9−Ta coordination bonds evenly distributed on four equivalent Ta@B_9 nonagonal faces, including four equivalent 10c-2e $B_9(\pi)$−Ta(d_σ) bonds in the first row and eight 10c-2e $B_9(\pi)$−Ta(d_δ) bonds in the second row. There exist thus one 10c-2e $B_9(\pi)$−Ta(d_σ) bond and two 10c-2e $B_9(\pi)$−Ta(d_δ) bonds over each Ta@B_9 nonagon, forming a local 6-π aromatic system over each quasi-planar Ta@B_9 unit to help stabilize the tetrahedral complex, similar to the situation in the experimentally observed aromatic inverse sandwich La_2B_8.[27] The remaining 18 valence electrons occupy nine totally delocalized 22c-2e bonds in the third row, including one 22c-2e S-type bond, three 22c-2e P-type bonds, and five 22c-2e D-type bonds. The nine 22c-2e bonds well correspond to the superatomic electronic configuration ($1S^21P^61D^{10}$) of T_d Ta_4B_{18} (**2**) depicted in Figure S5. As shown in Figure S6, T_d Nb_4B_{18} exhibits a similar bonding pattern. Such bonding patterns render spherical aromaticity to both T_d Ta_4B_{18} (**2**) and T_d Nb_4B_{18}, as evidenced by the calculated large negative nucleus-independent chemical shift[45,46] values of NICS = −141.9 and −124.9 ppm at their cage centers, respectively.

The spherical aromatic nature of T_d Ta_4B_{18} (**2**) is further evidenced by its iso-chemical shielding surfaces (ICSSs)[47,48] depicted in Figure 4a based on the calculated NICS-ZZ

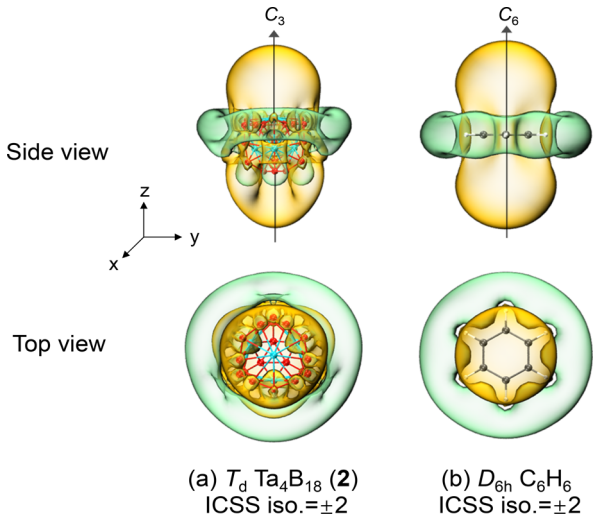

Figure 4. Comparison between the calculated iso-chemical shielding surfaces (ICSSs) of (a) Ta_4B_{18} (**2**) and (b) D_{6h} C_6H_6, with the corresponding NICS-ZZ components indicated. The C_3 axis of Ta_4B_{18} (**2**) and the C_6 axis of C_6H_6 are designated as the z axis in the vertical direction. Yellow regions stand for chemical shielding areas, while green areas represent chemical deshielding regions.

components, where the z axis is parallel to a C_3 molecular axis of the system to show the chemical shielding around the Ta@B_9 nonagon on the top, in comparison with the corresponding calculated ICSSs of benzene C_6H_6 in the C_6 direction (Figure 4b). The areas highlighted in yellow inside the Ta_4B_{18} tetrahedron and within about 1.0 A above the Ta centers in radial directions belong to chemical shielding regions with negative NICS-ZZ values, showing that the main aromatic contribution originates from Ta(5d)−B(2p) coordination

https://doi.org/10.1021/acsomega.1c00828
ACS Omega XXXX, XXX, XXX−XXX

interactions between the Ta centers and B_9 ligands. The chemical deshielding areas with positive NICS-ZZ values highlighted in green are located outside the Ta@B_9 nonagons in tangential directions. Interestingly, as clearly shown in Figure 4, the ICSSs of T_d Ta_4B_{18} (**2**) appears to be similar to those of benzene D_{6h} C_6H_6 in radial directions, well demonstrating the aromatic nature of the spherical tetrahedral complex.

Simulated IR, Raman, and UV−Vis Spectra. The infrared (IR), Raman, and UV−vis spectra of T_d Ta_4B_{18} (**2**) and T_d Nb_4B_{18} are computationally simulated in Figure 5 and Figure S7 to facilitate their spectral characterizations. As shown in Figure 5, Ta_4B_{18} (**2**) possesses four sharp IR peaks at 161(t_2), 310(t_2), 659(t_2), and 1082(t_2) cm^{-1} and five major Raman active vibrations at 329(e), 467(t_2), 622(a_1), 999(e), and 1236(a_1) cm^{-1}. The weak Raman peak at 223(a_1) cm^{-1} and strongest Raman peak at 622(a_1) cm^{-1} correspond to typical "radial breathing modes" (RBMs) of the cage-like structure, which can be used to characterize single-walled hollow boron nanostructures.[49] The simulated UV−vis spectrum of Ta_4B_{18} (**2**) with 150 excited states included in the calculations exhibits strong absorption peaks at 294, 393, and 409 nm, which mainly originate from electron transitions from the deep inner shells to the highly unoccupied molecular orbitals of Ta_4B_{18} (**2**). T_d Nb_4B_{18} exhibits similar spectral features to Ta_4B_{18} (**2**) (Figure S7).

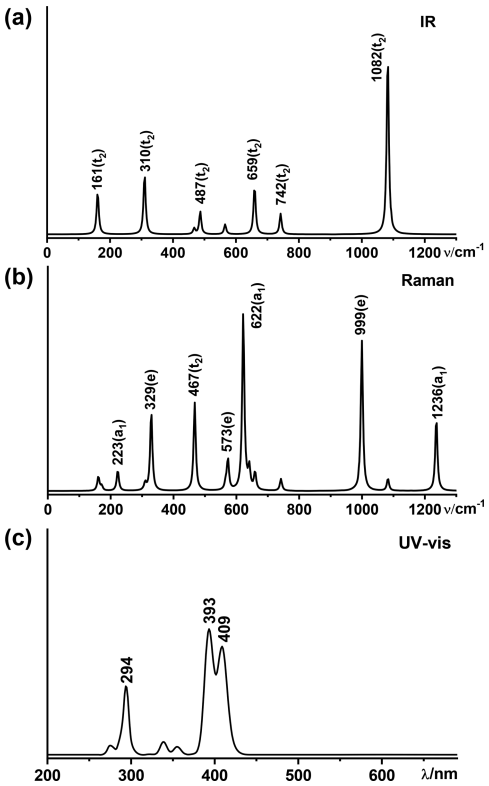

Figure 5. Simulated (a) IR, (b) Raman, and (c) UV−vis spectra of T_d Ta_4B_{18} (**2**) at the PBE0 level.

CONCLUSIONS

Based on extensive GM searches and first-principles theory calculations, we have proposed in this work the perfect spherical tetrahedral metallo-borospherenes T_d Ta_4B_{18} (**2**) and T_d Nb_4B_{18}, which possess the same tetrahedral symmetry as their carbon fullerene counterpart T_d C_{28}. T_d M_4B_{18} (M = Ta and Nb) appears to be spherically aromatic in nature, with 18 valence electrons occupying nine 22c-2e totally delocalized bonds following the superatomic electronic configuration of $1S^21P^61D^{10}$. Such highly stable spherically aromatic metallo-borospherene clusters may be synthesized and characterized in gas phases by laser ablations of Ta−B or Nb−B binary targets.[19−29,31] As the smallest tetra-metal-doped metallo-borospherenes reported to date, they are possible to be self-assembled to form novel 3D boron nanostructures.

THEORETICAL PROCEDURE

Extensive GM searches on Ta_4B_{18} and Nb_4B_{18} were performed using the Tsinghua Global Minimum (TGMin) package,[36,37] in conjunction with manual structural constructions based on the smallest metallo-borospherene D_{3h} $Ta_3B_{12}^-$ (**1**).[33] More than 1500 singlet or triplet stationary points were explored for each cluster at the PBE/DZVP level.[42] Low-lying isomers were then fully optimized at the PBE0[41] level with the 6-31+G* basis set[50] for B and the Stuttgart (2f1g) pseudopotential[51,52] for Ta and Nb using the Gaussian-16 program suite,[53] with vibrational frequencies checked to make sure that all isomers reported are true minima. The 10 lowest-lying isomers were subsequently reoptimized using the PBE0 functional with the aug-cc-pVTZ basis set[54,55] for B and the Stuttgart (2f1g) pseudopotential for Ta and Nb. Relative energies for the five lowest-lying isomers were further refined for Ta_4B_{18} using the more accurate coupled cluster method with triple excitations CCSD(T)[38−40] implemented in Molpro[56] with the basis set of 6-31G(d) for B and the Stuttgart (2f1g) pseudopotential for Ta. The calculations on the 3D Ta_3B_{15} crystal (**3**) were performed using the Vienna ab initio simulation package (VASP)[57,58] within the framework of the projector-augmented wave (PAW) pseudopotential method[59,60] and PBE generalized gradient approximation (GGA).[42,61] Natural bonding orbital analyses were performed using the NBO 6.0 program.[62] Nucleus-independent chemical shifts (NICS)[45,46] were calculated at the cage centers to assess the spherical aromaticity of tetrahedral metallo-borospherenes. The iso-chemical shielding surfaces (ICSSs)[47,48] were generated with the Multiwfn 3.7 code.[63] Chemical bonding was analyzed using the adaptive natural density partitioning (AdNDP) method,[43,43] which has been successfully applied to various organic and inorganic species.[2−10,18,19] Molecular dynamics (MD) simulations were carried out on T_d Ta_4B_{18} for 30 ps using a CP2K software suite.[64] The iso-surface maps of various orbitals and the iso-chemical shielding surfaces (ICSSs) were realized using the visual molecular dynamics (VMD) software.[65]

ASSOCIATED CONTENT

Supporting Information

The Supporting Information is available free of charge at https://pubs.acs.org/doi/10.1021/acsomega.1c00828.

Low-lying isomers of Ta_4B_{18} at the PBE0 and CCSD(T) levels (Figure S1); low-lying isomers of Nb_4B_{18} at the PBE0 and CCSD(T) levels (Figure S2); MD simulations of Ta_4B_{18} (**2**) at 1500 K and T_d Nb_4B_{18} at 1200 K (Figure S3); calculated band structures and projected densities of states (PDOS) of Ta_4B_{15} (**3**) at the PBE level (Figure S4); the superatomic electronic configuration ($1S^21P^61D^{10}$) of T_d Ta_4B_{18} (**2**) (Figure S5); AdNDP bonding patterns of T_d Nb_4B_{18} (Figure S6); simulated IR, Raman, and UV−vis spectra of T_d Nb_4B_{18} at the PBE0 level (Figure S7);

https://doi.org/10.1021/acsomega.1c00828
ACS Omega XXXX, XXX, XXX−XXX

optimized coordinates of T_d Ta_4B_{18} (**2**) and T_d Nb_4B_{18} at PBE0 (Table S1); and optimized coordinates (x, y, z) of the 3D Ta_4B_{15} (**3**) crystal at the PBE level (Table S2) (PDF)

AUTHOR INFORMATION

Corresponding Author

Si-Dian Li − *Institute of Molecular Science, Shanxi University, Taiyuan 030006, China;* orcid.org/0000-0001-5666-0591; Email: lisidian@sxu.edu.cn

Authors

Yu Zhang − *Institute of Molecular Science, Shanxi University, Taiyuan 030006, China*

Xiao-Qin Lu − *Institute of Molecular Science, Shanxi University, Taiyuan 030006, China*

Miao Yan − *Institute of Molecular Science, Shanxi University, Taiyuan 030006, China*

Complete contact information is available at: https://pubs.acs.org/10.1021/acsomega.1c00828

Notes

The authors declare no competing financial interest.

REFERENCES

(1) Cotton, F. A.; Wilkinson, G.; Murrillo, C. A.; Bochmann, M. *Advanced Inorganic Chemistry*, Wiley, New York, 6th edn, 1999.

(2) Wang, L. S. Photoelectron spectroscopy of size-selected boron clusters: from planar structures to borophenes and borospherenes. *Int. Rev. Phys. Chem.* **2016**, *35*, 69−142.

(3) Jian, T.; Chen, X.; Li, S.-D.; Boldyrev, A. I.; Li, J.; Wang, L.-S. Probing the structures and bonding of size-selected boron and doped-boron clusters. *Chem. Soc. Rev.* **2019**, *48*, 3550−3591.

(4) Zhai, H. J.; Zhao, Y. F.; Li, W. L.; Chen, Q.; Bai, H.; Hu, H. S.; Piazza, Z. A.; Tian, W. J.; Lu, H. G.; Wu, Y. B.; Mu, Y. W.; Wei, G. F.; Liu, Z. P.; Li, J.; Li, S. D.; Wang, L. S. Observation of an all-boron fullerene. *Nat. Chem.* **2014**, *6*, 727−731.

(5) Chen, Q.; Li, W. L.; Zhao, Y. F.; Zhang, S. Y.; Hu, H. S.; Bai, H.; Li, H. R.; Tian, W. J.; Lu, H. G.; Zhai, H. J.; Li, S. D.; Li, J.; Wang, L. S. Experimental and theoretical evidence of an axially chiral borospherene. *ACS Nano* **2015**, *9*, 754−760.

(6) Chen, Q.; Zhang, S. Y.; Bai, H.; Tian, W. J.; Gao, T.; Li, H. R.; Miao, C. Q.; Mu, Y. W.; Lu, H. G.; Zhai, H. J.; Li, S. D. Cage-Like B41 (+) and B42 (2+) : New Chiral Members of the Borospherene Family. *Angew. Chem., Int. Ed.* **2015**, *54*, 8160−8164.

(7) Wang, Y. J.; Zhao, Y. F.; Li, W. L.; Jian, T.; Chen, Q.; You, X. R.; Ou, T.; Zhao, X. Y.; Zhai, H. J.; Li, S. D.; Li, J.; Wang, L. S. Observation and characterization of the smallest borospherene, B28(−) and B28. *J. Chem. Phys.* **2016**, *144*, No. 064307.

(8) Li, H. R.; Jian, T.; Li, W. L.; Miao, C. Q.; Wang, Y. J.; Chen, Q.; Luo, X. M.; Wang, K.; Zhai, H. J.; Li, S. D.; Wang, L. S. Competition between quasi-planar and cage-like structures in the B29(−) cluster: photoelectron spectroscopy and ab initio calculations. *Phys. Chem. Chem. Phys.* **2016**, *18*, 29147−29155.

(9) Bai, H.; Chen, T. T.; Chen, Q.; Zhao, X. Y.; Zhang, Y. Y.; Chen, W. J.; Li, W. L.; Cheung, L. F.; Bai, B.; Cavanagh, J.; Huang, W.; Li, S. D.; Li, J.; Wang, L. S. Planar B_{41}^- and B_{42}^- clusters with double-hexagonal vacancies. *Nanoscale* **2019**, *11*, 23286−23295.

(10) Bai, H.; Chen, Q.; Zhai, H. J.; Li, S. D. Endohedral and exohedral metalloborospherenes: M@B40 (M=Ca, Sr) and M&B40 (M=Be, Mg). *Angew. Chem., Int. Ed.* **2015**, *54*, 941−945.

(11) Jin, P.; Hou, Q.; Tang, C.; Chen, Z. Computational investigation on the endohedral borofullerenes M@B40 (M = Sc, Y, La). *Theor. Chem. Acc.* **2015**, *134*, 044001.

(12) Li, H. R.; Liu, H.; Tian, X. X.; Zan, W. Y.; Mu, Y. W.; Lu, H. G.; Li, J.; Wang, Y. K.; Li, S. D. Structural transition in metal-centered boron clusters: from tubular molecular rotors Ta@B21 and Ta@B22(+) to cage-like endohedral metalloborospherene Ta@B22. *Phys. Chem. Chem. Phys.* **2017**, *19*, 27025−27030.

(13) Yu, T.; Gao, Y.; Xu, D.; Wang, Z. Actinide endohedral boron clusters: A closed-shell electronic structure of U@B40. *Nano Res.* **2017**, *11*, 354−359.

(14) Chopra, S. Boron fullerenes, Bn (n=20, 30, 38, 40, 50, 60): First principle calculations of electronic and optical properties. *J. Mol. Graphics Modell.* **2018**, *84*, 90−95.

(15) Chopra, S.; Lu, T. A DFT/TDDFT and QTAIM based investigation of the titanium-doped Boron-38 cluster. *Theor. Chem. Acc.* **2020**, *139*, 1−8.

(16) Oger, E.; Crawford, N. R. M.; Kelting, R.; Weis, P.; Kappes, M. M.; Ahlrichs, R. Boron cluster cations: transition from planar to cylindrical structures. *Angew. Chem., Int. Ed.* **2007**, *46*, 8503−8506.

(17) Sai, L.; Wu, X.; Gao, N.; Zhao, J.; King, R. B. Boron clusters with 46, 48, and 50 atoms: competition among the core-shell, bilayer and quasi-planar structures. *Nanoscale* **2017**, *9*, 13905−13909.

(18) Pei, L.; Ma, Y. Y.; Yan, M.; Zhang, M.; Yuan, R. N.; Chen, Q.; Zan, W. Y.; Mu, Y. W.; Li, S. D. Bilayer B54, B60, and B62 Clusters in a Universal Structural Pattern. *Eur. J. Inorg. Chem.* **2020**, *2020*, 3296−3301.

(19) Chen, W. J.; Ma, Y. Y.; Chen, T. T.; Ao, M. Z.; Yuan, D. F.; Chen, Q.; Tian, X. X.; Mu, Y. W.; Li, S. D.; Wang, L. S. B48(−): a bilayer boron cluster. *Nanoscale* **2021**, 3868.

(20) Romanescu, C.; Galeev, T. R.; Li, W. L.; Boldyrev, A. I.; Wang, L. S. Aromatic metal-centered monocyclic boron rings: Co(c)B8- and Ru(c)B9. *Angew. Chem., Int. Ed.* **2011**, *50*, 9334−9337.

(21) Galeev, T. R.; Romanescu, C.; Li, W. L.; Wang, L. S.; Boldyrev, A. I. Observation of the highest coordination number in planar species: decacoordinated Ta(c)B10(−) and Nb(c)B10(−) anions. *Angew. Chem., Int. Ed.* **2012**, *51*, 2101−2105.

(22) Jian, T.; Li, W. L.; Popov, I. A.; Lopez, G. V.; Chen, X.; Boldyrev, A. I.; Li, J.; Wang, L. S. Manganese-centered tubular boron cluster - MnB16 (−): A new class of transition-metal molecules. *J. Chem. Phys.* **2016**, *144*, 154310.

(23) Popov, I. A.; Jian, T.; Lopez, G. V.; Boldyrev, A. I.; Wang, L. S. Cobalt-centred boron molecular drums with the highest coordination number in the CoB16- cluster. *Nat. Commun.* **2015**, *6*, 8654.

(24) Jian, T.; Li, W. L.; Chen, X.; Chen, T. T.; Lopez, G. V.; Li, J.; Wang, L. S. Competition between drum and quasi-planar structures in RhB18(−): motifs for metallo-boronanotubes and metallo-borophenes. *Chem. Sci.* **2016**, *7*, 7020−7027.

(25) Li, W. L.; Jian, T.; Chen, X.; Li, H. R.; Chen, T. T.; Luo, X. M.; Li, S. D.; Li, J.; Wang, L. S. Observation of a metal-centered B2-Ta@B18(−) tubular molecular rotor and a perfect Ta@B20(−) boron drum with the record coordination number of twenty. *Chem. Commun.* **2017**, *53*, 1587−1590.

(26) Li, W.-L.; Xie, L.; Jian, T.; Romanescu, C.; Huang, X.; Wang, L.-S. Hexagonal Bipyramidal [Ta2B6]−/0Clusters: B6Rings as Structural Motifs. *Am. Ethnol.* **2014**, *126*, 1312−1316.

(27) Li, W. L.; Chen, T. T.; Xing, D. H.; Chen, X.; Li, J.; Wang, L. S. Observation of highly stable and symmetric lanthanide octa-boron inverse sandwich complexes. *Proc. Natl. Acad. Sci. U. S. A.* **2018**, *115*, E6972−E6977.

(28) Chen, T. T.; Li, W. L.; Li, J.; Wang, L. S. [La(eta (x) -B x)La](−) (x = 7-9): a new class of inverse sandwich complexes. *Chem. Sci.* **2019**, *10*, 2534−2542.

(29) Chen, T. T.; Li, W. L.; Chen, W. J.; Li, J.; Wang, L. S. La3B14(−): an inverse triple-decker lanthanide boron cluster. *Chem. Commun.* **2019**, *55*, 7864−7867.

(30) Lu, X. Q.; Chen, Q.; Tian, X. X.; Mu, Y. W.; Lu, H. G.; Li, S. D. Predicting lanthanide boride inverse sandwich tubular molecular rotors with the smallest core-shell structure. *Nanoscale* **2019**, *11*, 21311−21316.

(31) Chen, T. T.; Li, W. L.; Chen, W. J.; Yu, X. H.; Dong, X. R.; Li, J.; Wang, L. S. Spherical trihedral metallo-borospherenes. *Nat. Comm.* **2020**, *11*, 2766.

(32) Zhao, X.-Y.; Yan, M.; Wei, Z.; Li, S.-D. Donor−acceptor duality of the transition-metal-like B2 core in core−shell-like metallo-borospherenes La3&[B2@B17]− and La3&[B2@B18]−. *RSC Adv.* **2020**, *10*, 34225−34230.
(33) Zhang, Y.; Zhao, X.-Y.; Yan, M.; Li, S.-D. From inverse sandwich Ta2B7+ and Ta2B8 to spherical trihedral Ta3B12−: prediction of the smallest metallo-borospherene. *RSC Adv.* **2020**, *10*, 29320−29325.
(34) Gao, Y.; Zeng, X. C. M4 @Si28 (M=Al,Ga): metal-encapsulated tetrahedral silicon fullerene. *J. Chem. Phys.* **2005**, *123*, 204325.
(35) Guo, T.; Diener, M. D.; Chai, Y.; Alford, M. J.; Haufler, R. E.; McClure, S. M.; Ohno, T.; Weaver, J. H.; Scuseria, G. E.; Smalley, R. E. Uranium stabilization of c28: a tetravalent fullerene. *Science* **1992**, *257*, 1661−1664.
(36) Zhao, Y.; Chen, X.; Li, J. TGMin: A global-minimum structure search program based on a constrained basin-hopping algorithm. *Nano Res.* **2017**, *10*, 3407−3420.
(37) Chen, X.; Zhao, Y.-F.; Wang, L.-S.; Li, J. Recent progresses of global minimum searches of nanoclusters with a constrained Basin-Hopping algorithm in the TGMin program. *Comput. Theor. Chem.* **2017**, *1107*, 57−65.
(38) Čížek, J. On the Use of the Cluster Expansion and the Technique of Diagrams in Calculations of Correlation Effects in Atoms and Molecules. *Adv. Chem. Phys.* **1969**, *14*, 35−89.
(39) Purvis, G. D., III; Bartlett, R. J. A full coupled-cluster singles and doubles model: The inclusion of disconnected triples. *J. Chem. Phys.* **1982**, *76*, 1910−1918.
(40) Raghavachari, K.; Trucks, G. W.; Pople, J. A.; Head-Gordon, M. A fifth-order perturbation comparison of electron correlation theories. *Chem. Phys. Lett.* **1989**, *157*, 479−483.
(41) Adamo, C.; Barone, V. Toward reliable density functional methods without adjustable parameters: The PBE0 model. *J. Chem. Phys.* **1999**, *110*, 6158−6170.
(42) Perdew, J. P.; Burke, K.; Ernzerhof, M. Generalized Gradient Approximation Made Simple. *Phys. Rev. Lett.* **1996**, *77*, 3865−3868.
(43) Zubarev, D. Y.; Boldyrev, A. I. Developing paradigms of chemical bonding: adaptive natural density partitioning. *Phys. Chem. Chem. Phys.* **2008**, *10*, 5207−5217.
(44) Tkachenko, N. V.; Boldyrev, A. I. Chemical bonding analysis of excited states using the adaptive natural density partitioning method. *Phys. Chem. Chem. Phys.* **2019**, *21*, 9590−9596.
(45) Schleyer, P. V. R.; Maerker, C.; Dransfeld, A.; Jiao, H.; van Eikema Hommes, N. J. R. Nucleus-Independent Chemical Shifts: A Simple and Efficient Aromaticity Probe. *J. Am. Chem. Soc.* **1996**, *118*, 6317−6318.
(46) Chen, Z.; Wannere, C. S.; Corminboeuf, C.; Puchta, R.; Schleyer, P. V. S. Nucleus-independent chemical shifts (NICS) as an aromaticity criterion. *Chem. Rev.* **2005**, *105*, 3842−3888.
(47) Klod, S.; Kleinpeter, E. Ab initio calculation of the anisotropy effect of multiple bonds and the ring current effect of arenes—application in conformational and configurational analysis. *J. Chem. Soc. Perkin Trans 2* **2001**, 1893−1898.
(48) Kleinpeter, E.; Klod, S.; Koch, A. Visualization of through space NMR shieldings of aromatic and anti-aromatic molecules and a simple means to compare and estimate aromaticity. *J. Mol. Struct.: THEOCHEM* **2007**, *811*, 45−60.
(49) Ciuparu, D.; Klie, R. F.; Zhu, Y.; Pfefferle, L. Synthesis of Pure Boron Single-Wall Nanotubes. *J. Phys. Chem. B* **2004**, *108*, 3967−3969.
(50) Feller, D. The role of databases in support of computational chemistry calculations. *J. Comput. Chem.* **1996**, *17*, 1571.
(51) Andrae, D.; Huermann, U.; Dolg, M.; Stoll, H.; Preu, H. Energy-adjustedab initio pseudopotentials for the second and third row transition elements. *Theor. Chim. Acta* **1990**, *77*, 123−141.
(52) Martin, J. M. L.; Sundermann, A. Correlation consistent valence basis sets for use with the Stuttgart−Dresden−Bonn relativistic effective core potentials: The atoms Ga−Kr and In−Xe. *J. Chem. Phys.* **2001**, *114*, 3408−3420.
(53) M. J., Frisch, G. W., Trucks, H. B., Schlegel, G. E., Scuseria, M. A., Robb, J. R., Cheeseman, G., Scalmani, V., Barone, G. A., Petersson, H., Nakatsuji, et al., *Gaussian 16, Revision A.03*, Gaussian Inc., Wallingford, CT, 2016.
(54) Dunning, T. H. Gaussian basis sets for use in correlated molecular calculations. I. The atoms boron through neon and hydrogen. *J. Chem. Phys.* **1989**, *90*, 1007−1023.
(55) Kendall, R. A.; Dunning, T. H.; Harrison Jr, R. J. Electron affinities of the first-row atoms revisited. Systematic basis sets and wave functions. *J. Chem. Phys.* **1992**, *96*, 6796−6806.
(56) Werner, H.-J.; Knowles, P. J.; Knizia, G.; Manby, F. R.; Schütz, M. Molpro: a general-purpose quantum chemistry program package. *WIREs Comput. Mol. Sci.* **2012**, *2*, 242−253.
(57) Kresse, G.; Furthmüller, J. Efficiency of ab-initio total energy calculations for metals and semiconductors using a plane-wave basis set. *Comput. Mater. Sci.* **1996**, *6*, 15−50.
(58) Kresse, G.; Fürthmuller, J. Efficient iterative schemes for ab initio total-energy calculations using a plane-wave basis set. *Phys. Rev B* **1996**, *54*, 11169−11186.
(59) Blochl, P. E. Projector augmented-wave method. *Phys. Rev. B* **1994**, *50*, 17953−17979.
(60) Kresse, G.; Joubert, D. From ultrasoft pseudopotentials to the projector augmented-wave method. *Phys. Rev. B* **1999**, *59*, 1758−1775.
(61) Perdew, J. P.; Burke, K.; Ernzerhof, M. Generalized Gradient Approximation Made Simple. *Phys. Rev. Lett.* **1997**, *78*, 1396−1396.
(62) Glendening, E. D.; Landis, C. R.; Weinhold, F. NBO 6.0: natural bond orbital analysis program. *J. Comput. Chem.* **2013**, *34*, 1429−1437.
(63) Lu, T.; Chen, F. Multiwfn: a multifunctional wavefunction analyzer. *J. Comput. Chem.* **2012**, *33*, 580−592.
(64) VandeVondele, J.; Krack, M.; Mohamed, F.; Parrinello, M.; Chassaing, T.; Hutter, J. Quickstep: Fast and accurate density functional calculations using a mixed Gaussian and plane waves approach. *Comput. Phys. Commun.* **2005**, *167*, 103−128.
(65) Koradi, R.; Billeter, M.; Wüthrich, K. MOLMOL: A program for display and analysis of macromolecular structures. *J. Mol. Graph.* **1996**, *14*, 51−55.

https://doi.org/10.1021/acsomega.1c00828
ACS Omega XXXX, XXX, XXX−XXX